Research Article

Effect of the Number of Nozzles of Swirl Flow Generator Utilized in Flat Plate Solar Collector: An Entropic Analysis

Yan Cao,[1] **Hamdi Ayed** ,[2] **Tuqa Abdulrazzaq,**[3] **Taza Gul,**[4] **Abdul Bariq** ,[5]
and Belgacem Bouallegue[6]

[1]*School of Mechatronic Engineering, Xi'an Technological University, Xi'an 710021, China*
[2]*Department of Civil Engineering, College of Engineering, King Khalid University, Abha 61421, Saudi Arabia*
[3]*Petroleum and Gas Engineering Department, University of Thi-Qar, Nassiriya 64001, Iraq*
[4]*Department of Mathematics, City University of Science and Information Technology, Peshawar 25000, Khyber, Pakhtunkhwa, Pakistan*
[5]*Department of Mathematics, Laghman University, Mehtarlam City, Laghman Province of Afghanistan, Afghanistan*
[6]*Department of Computer Engineering, College of Computer Science, King Khalid University, Abha, Saudi Arabia*

Correspondence should be addressed to Abdul Bariq; abdulbariq.maths@lu.edu.af

The numerical model of the pipes of a flat plate solar collector (FPSC) with several nozzles has been investigated in the present study. Indeed, the effect of the number of nozzles of the swirl generator on the entropic characteristics has been evaluated. The nozzles were applied for improving the performance of FPSC. For evaluating the proposed system based on the entropy concept, the effect of injection angle and mass flow rate has been considered. The selected injection angles were 30°, 45°, 60°, and 90°. Also, the total mass flow rates entered from all of the nozzles were 0.2 kg/s, 1 kg/s, and 2 kg/s. The effect of said variables on frictional and thermal entropy generations was analyzed; then, the overall energetic-entropic performance of the system was predicted using several dimensionless parameters including N_E, N_S, Nu^*, and heat transfer improvement (HTI). Moreover, Witte-Shamsundar efficiency (η_{W-S}) was applied to pinpoint the efficiency of the system. The highest value of HTI and η_{W-S} was 1.7 and 0.9 that achieved by "single-nozzle; A90-D50-N12.5-M0.2" and "quad-nozzle; A30-D50-N12.5-M2," respectively.

1. Introduction

In order to meet the growing energy, it needs different sources of energies that has been considered [1, 2]. To this end, various technologies have been developed [3, 4]. The heat is a more accessible and transformable types of energy [5, 6]. Solar thermal is a new and renewable thermal source that recently lots of systems have been designed and developed for attaining its efficient utilization [7, 8]. This clean energy source even can be used for running power plants [9, 10]. To this end, the improvement of solar thermal systems has been done from both microscopic [11] and macroscopic viewpoints and in combination with other systems [12, 13]. One of the main irreversibility sources [14, 15] is

the thermal factor; so, the heat transfer quality of the any of thermal systems can be assessed by the entropy concept [16, 17]. Pourhedayat et al. [18] studied the effect of using triangular vortex generators inside the pipe on thermal performance and exergy destruction. Different geometrical and structural characteristics of vinglets including winglet plate angle and latitudinal pitch were changed. Results showed that when the pitch equals 20 mm, the highest heat transfer can be achieved. Jalili et al. [19] studied environmental economic analysis of a geothermal-based power plant by the energy concept which is a function of exergetic characteristics of the system. In this study, flash and the binary geothermal system were integrated with each other as a hybrid heat and power generation cycle. They found that the energetic

efficiency of the system is 54% while the highest achieved exergetic efficiency is 64%. Al-Turki et al. [20] proposed various parallel/nonparallel plate heat exchangers and numerically investigated the thermal, frictional, and the exergetic characteristics of each of them. It was inferred that different arrangements of flow direction and plates' configurations caused distinct entropy generation. Furthermore, the maximum Nu was achieved when hot and cold streams passed through convergent and divergent channels. Cao et al. [21] conducted a numerical simulation to analyze the effect of making annular depressions on the inner and outer wall of the tube-in-tube helical heat exchanger on the entropy generation. Different configurations and locations of annular depression were tested. Reported results demonstrated that although the case "*d*" makes the highest heat transfer, it generates the greatest entropy. In another work, Cao et al. [22] selected a helically coiled double tube heat exchanger to investigate R134a flow condensation by entropy generation study as well as sensitivity analysis. Different geometrical and flow conditions were taken into account. It was found that considered flow conditions are sensitive to alteration when mass velocity is considerable ($G \geq 300 \, \text{kg.m}^{-2}.\text{s}^{-1}$), and the vapor quality at the inlet section is $x \geq 0.5$ also for Tsat≤46°C. Li et al. [23] performed thermal analysis on the channel with solid bodies for making swirl flow structure in this study, and different Re numbers and swirl chamber heights were considered. The highest heat transfer and lowest pressure drop achieved when channel height was 19 mm.

There are two major distinctive aspects of the present work with the others that make this study to be novel: (i) using nozzles for inducing swirl flow inside FPSCs and (ii) embedding pipes inside the phase change material (PCM) instead of having contact with absorber plate. No study has explored the effect of equipping the pipes of FPSC with the swirl generator to understand the performance of it based on the first and second laws of thermodynamics. Moreover, in the new design of FPSC, the pipes are embedded inside the PCM so that all area of pipes is subjected to the uniform temperature, while in the conventional type of FPSC, top semiwall of pipes is in contact to the absorber plate, and only this section receives heat. In fact, in this new design absorber plate transfer, the receiver heat to a media like PCM and this media acts as both energy storage and provides uniform heat flux to all part of the pipes. In this study, by considering the multiple-nozzle swirl generator new method that has been introduced for improving the efficiency of FPSC, number of the nozzles of swirl generator was varied from one to four nozzles; also, the sum of mass flow rate of all nozzles varied from 0.2 kg/s to 2 kg/s. The performance of the system was analyzed based on the second law of thermodynamics.

2. Model Description and Calculation Method

A new design has been proposed for FPSC in which the pipes of FPSC have been equipped with the swirl generator. In this study, the swirl flow is induced inside the piping system of FPSC by designed nozzles as shown in Figure 1. The

number of employed nozzles is a key parameter; so, in this study, swirl generators with "single," "dual," "triple," and "quad" nozzles were tested to understand the effect of each of them on the entropic behavior of the system. According to Figure 1, except inlet and outlet sections, all of the surfaces have been defined as a wall. Only the peripheral surface of the cylindrical tube was subjected to the constant temperature (to simulate the working condition of FPSC) while the rest of the walls was assumed to be adiabatic. The overall mass flow rate was varied from 0.2 kg/s to 2 kg/s that this flow rate was divided among nozzles proportional to the number of them. Unlike other dimensions of the tube, its length had a constant size (700 mm). This study eliminates the need for using advanced technologies for enhancing performance of the system [24, 25].

To analyze the system based on the obtained data from numerical calculations following calculation method was adopted, the formulation of the total entropy balance for an open thermodynamic system is [7]

$$\sum \frac{\dot{Q}_k}{T_k} + \sum \dot{m}_i s_i - \sum \dot{m}_0 s_0 + \dot{S}_{\text{gen}} = \frac{dS_{\text{cv}}}{dt}. \quad (1)$$

The studied system is not transient (it operates under steady state condition); so,

$$\frac{dS_{\text{cv}}}{dt} = 0. \quad (2)$$

By replacing Eq. (2) in Eq. (1) [7],

$$\dot{S}_{\text{gen}} = \sum \frac{\dot{Q}_k}{T_k} + \sum \dot{m}_i s_i - \sum \dot{m}_0 s_0. \quad (3)$$

Based on mass balance [26],

$$\sum \dot{m}_i = \sum \dot{m}_o. \quad (4)$$

For "single-nozzle" swirl generator, mass balance can be expressed as [26]

$$\dot{m}_{\text{Nozzle\#1}} = \dot{m}_o. \quad (5)$$

When this generalized for swirl generator with "*n*" nozzles [26],

$$\dot{m}_{total} = \sum_{n=1}^{4} \dot{m}_n. \quad (6)$$

By substituting Eq. (6) in Eq. (3) [7],

$$\frac{\dot{Q}_k}{T_k} + \dot{m}_{\text{total}}(S_i - S_o) = \dot{S}_{\text{gen}}. \quad (7)$$
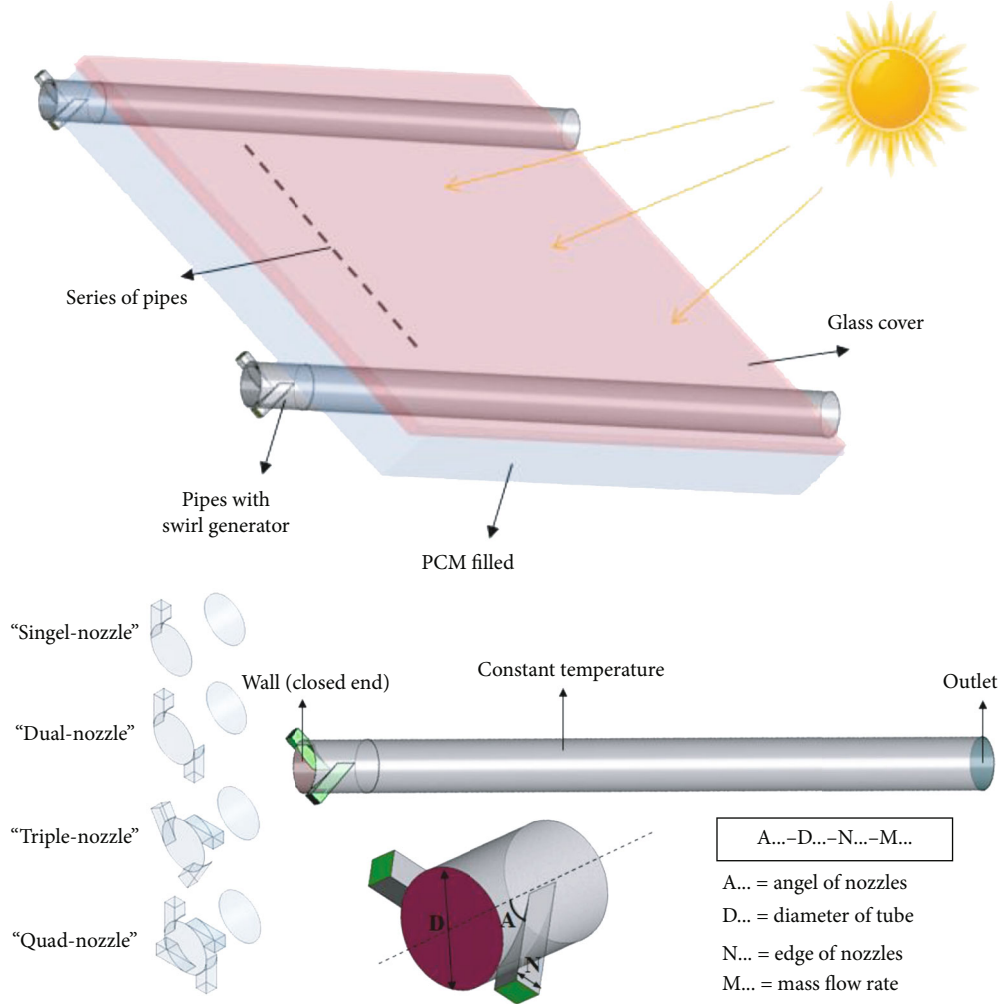
FIGURE 1: Diagram of flat plate solar collector with new designed pipes.

The involved irreversibility sources in this system are thermal and frictional sources; hence. entropy generation can be expressed as [20, 21]

$$\dot{S}_{\text{gen}} = \dot{S}_{\text{gen, Thermal}} + \dot{S}_{\text{gen,Frictional}}. \tag{8}$$

For $\dot{S}_{\text{gen, Thermal}}$,

$$\dot{S}_{\text{gen,thermal}} = \left(\dot{m}\, C_p\right) \ln \frac{T_{\text{out}}}{T_{\text{in}}}. \tag{9}$$

For $\dot{S}_{\text{gen,Frictional}}$,

$$\dot{S}_{\text{gen,Frictional}} = \frac{\dot{m}}{\rho}\, \Delta P \frac{\ln\left(T_0/T_{\text{in}}\right)}{\left(T_0 - T_{\text{in}}\right)}. \tag{10}$$

Replacing Eq. (8) and Eq. (9) into Eq. (10), the total equation of entropy generation can be achieved [7]:

$$\dot{S}_{\text{gen}} = \left(\dot{m}\, C_p\right)\ln\ln\frac{T_{\text{out}}}{T_{\text{in}}} + \frac{\dot{m}}{\rho}\, \Delta P \frac{\ln\left(T_0/T_{\text{in}}\right)}{\left(T_0 - T_{\text{in}}\right)}. \tag{11}$$

Dimensionless form of Eq. (11) can be calculated as follows [20]:

$$N_s = \frac{\dot{S}_{\text{gen}}}{\dot{m}\, C_p}. \tag{12}$$

To find the ratio of entropy generation number of modified ($N_{s,m}$) to unmodified system ($N_{s,\text{um}}$), the nondimensional parameter N_E has defined as follows [20]:

$$N_E = \frac{N_{s,m}}{N_{s,\text{um}}}. \tag{13}$$

Similarly, Nu^* is the ratio of Nu of the modified (Nu_m) to the unmodified (Nu_{um}) system that can be obtained by [20, 27]

$$Nu^* = \frac{Nu_m}{Nu_{um}}. \tag{14}$$

To obtain the ratio of Nu^* to N_E, the following parameter was considered [7, 8]:

$$HTI\ index = N_H = \frac{Nu^*}{N_E}. \tag{15}$$

Also, Witte-Shamsundar efficiency (η_{W-S}) can be calculated by [7, 8]

$$\eta_{W-S} = \frac{\dot{Q} - T_0 S'_{gen}}{\dot{Q}} = 1 - \frac{\dot{I}}{\dot{Q}} = \frac{\text{Net transferred energy}}{\text{Total received energy}}. \tag{16}$$

3. Numerical Modeling

3.1. Governing Equations and Assumptions. Governing equations on this simulation are as follows [26]:

(i) Continuity equation:

$$\frac{1}{r}\frac{\partial}{\partial r}(ru_r) + \frac{1}{r}\frac{\partial u_\theta}{\partial \theta} + \frac{\partial u_z}{\partial z} = 0. \tag{17}$$

(ii) Momentum equation:

r-component:

$$\rho\left[u_r\frac{\partial u_r}{\partial r} + \frac{u_\theta}{r}\frac{\partial u_r}{\partial \theta} + u_z\frac{\partial u_r}{\partial z} - \frac{u_\theta^2}{r}\right]$$
$$= -\frac{\partial p}{\partial r} + \mu\left[\frac{\partial}{\partial r}\left(\frac{1}{r}\frac{\partial}{\partial r}(ru_r)\right) + \frac{1}{r^2}\frac{\partial^2 u_r}{\partial \theta^2} + \frac{\partial^2 u_r}{\partial z^2} - \frac{2}{r^2}\frac{\partial u_\theta}{\partial \theta}\right]. \tag{18}$$

θ-component:

$$\rho\left[u_r\frac{\partial u_\theta}{\partial r} + \frac{u_\theta}{r}\frac{\partial u_\theta}{\partial \theta} + u_z\frac{\partial u_\theta}{\partial z} + \frac{u_r u_\theta}{r}\right]$$
$$= -\frac{1}{r}\frac{\partial p}{\partial r} + \mu\left[\frac{\partial}{\partial r}\left(\frac{1}{r}\frac{\partial}{\partial r}(ru_\theta)\right) + \frac{1}{r^2}\frac{\partial^2 u_\theta}{\partial \theta^2} + \frac{\partial^2 u_\theta}{\partial z^2} + \frac{2}{r^2}\frac{\partial u_r}{\partial \theta}\right]. \tag{19}$$

z-component:

$$\rho\left[u_r\frac{\partial u_z}{\partial r} + \frac{u_\theta}{r}\frac{\partial u_z}{\partial \theta} + u_z\frac{\partial u_z}{\partial z}\right]$$
$$= -\frac{\partial p}{\partial z} + \mu\left[\frac{1}{r}\frac{\partial}{\partial r}\left(r\frac{\partial u_z}{\partial r}\right) + \frac{1}{r^2}\frac{\partial^2 u_z}{\partial \theta^2} + \frac{\partial^2 u_z}{\partial z^2}\right]. \tag{20}$$

(iii) Energy equation:

$$\rho c_p\left[u_r\frac{\partial T}{\partial r} + \frac{u_\theta}{r}\frac{\partial T}{\partial \theta} + u_z\frac{\partial u_r}{\partial z}\right]$$
$$= k\left[\frac{1}{r}\frac{\partial}{\partial r}\left(r\frac{\partial T}{\partial r}\right) + \frac{1}{r^2}\frac{\partial^2 T}{\partial \theta^2} + \frac{\partial^2 T}{\partial z^2}\right]. \tag{21}$$

Made assumptions and defined boundary conditions are

(i) Side wall of cylindrical pipe was under constant wall temperature of 360°C

(ii) Inlet temperature was 300°C

(iii) Except inlet, outlet, and peripheral wall of pipe the rest of walls had no heat and mass flux

(iv) Inlet boundary condition was selected as "mass flow rate"

(v) Outlet boundary condition was "pressure-outlet"

(vi) All walls were smooth with "no-slip" boundary condition

(vii) It was considered that the temperature changes have no effect on the properties of materials

3.2. Numerical Scheme, Validation, and Grid Independency. This simulation was done based on the finite volume method (FVM). ANSYS CFX 15 was used for simulating the 3D model of problem. Swirl flow is a turbulent flow; so, k-omega SST model was adopted for modeling swirl flow accurately. This turbulent model (k-omega SST) provides more accurate results since it blends k-epsilon and k-omega models to take near wall and far wall regions into account. In the real conditions due to the swirl nature of flow, the hydraulic conditions in the core of pipe are very different than near-wall regions. High-resolution scheme and fourth-order pressure velocity coupling algorithm were employed. The calculation process stopped when the residuals of continuity, momentum, and energy were less than 10^{-5}, 10^{-5}, and 10^{-8}, respectively. Four different mesh structures with the number of elements of 822436, 1356287, 1808762, and 2209345 were used for testing the grid independency [28]. As presented in Figure 2(a), total pressure changes are not meaningful after 1356287; so, this was selected as the grid structure of the computational domain. Figure 2(c) shows the validation results based on U/U_{ave}. Result accuracy verification was checked by the results provided by Chan and Dahir [29]. The considered conditions were Re = 12500, the ratio of nozzle momentum flux to tube momentum flux (M_t/M_T), and ration of tube length to tube diameter of 10 ($x/D = 10$). These applied conditions were exactly taken by Chan and Dahir [29]. According to this comparison, obtained results have an excellent agreement, and numerical settings can be used for intended simulations. The CFD process flowchart of numerical scheme has been provided in Figure 2(c).

4. Results and Discussions

4.1. Entropy Generation Analysis. Entropy generation due to thermal source for cases with a different number of nozzles
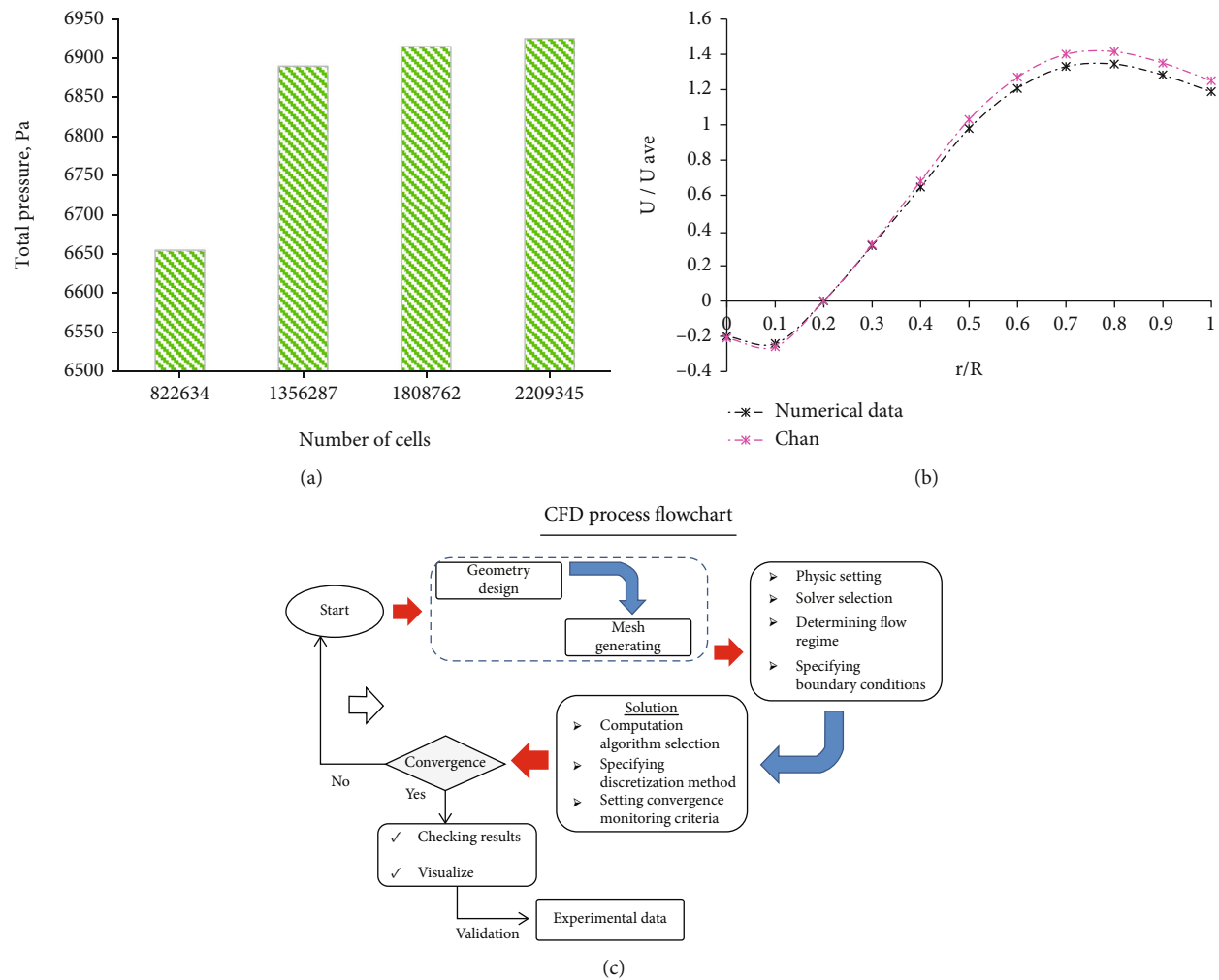
(a)

(b)

(c)

Figure 2: (a) Grid independency results. (b) Validation results. (c) CFD process flowchart.
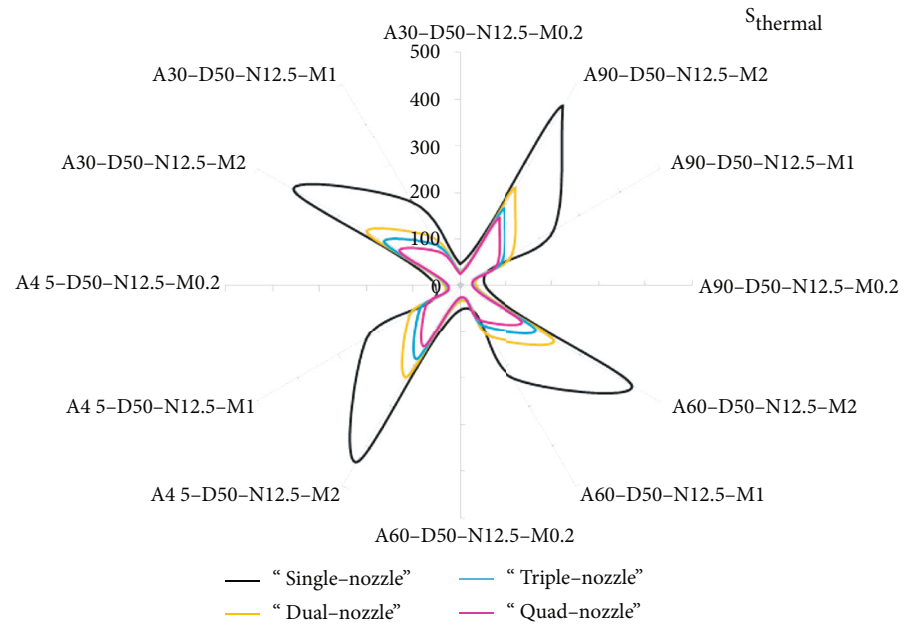

Figure 3: Entropy generation due to thermal source.

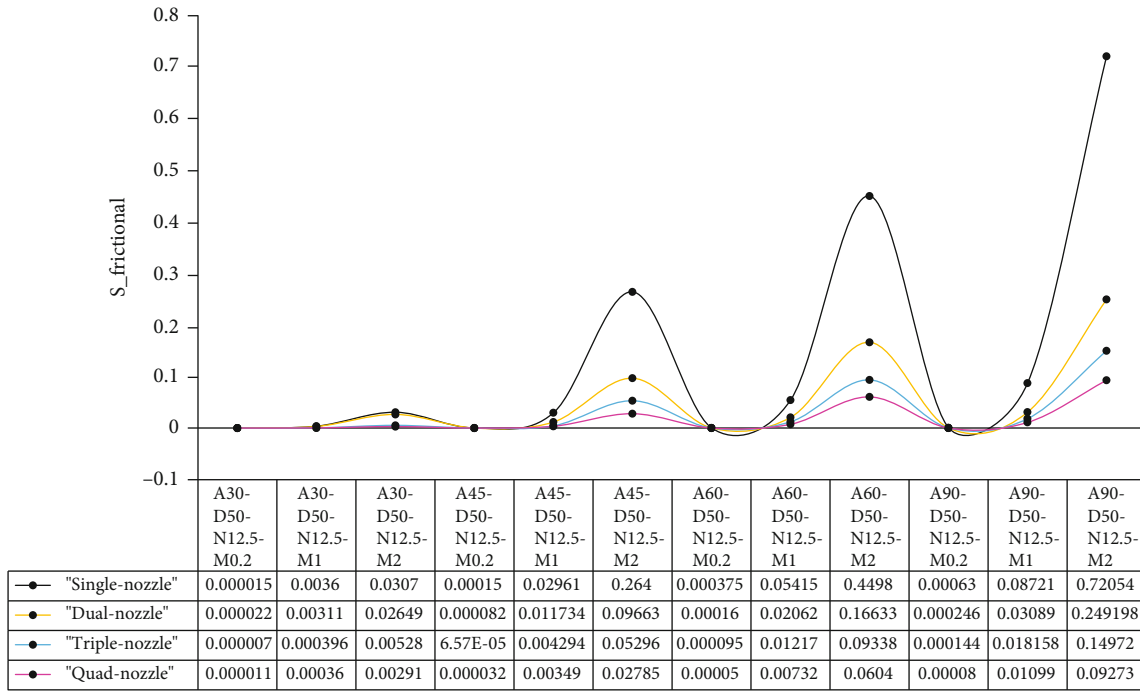|	A30-D50-N12.5-M0.2	A30-D50-N12.5-M1	A30-D50-N12.5-M2	A45-D50-N12.5-M0.2	A45-D50-N12.5-M1	A45-D50-N12.5-M2	A60-D50-N12.5-M0.2	A60-D50-N12.5-M1	A60-D50-N12.5-M2	A90-D50-N12.5-M0.2	A90-D50-N12.5-M1	A90-D50-N12.5-M2
"Single-nozzle"	0.000015	0.0036	0.0307	0.00015	0.02961	0.264	0.000375	0.05415	0.4498	0.00063	0.08721	0.72054
"Dual-nozzle"	0.000022	0.00311	0.02649	0.000082	0.011734	0.09663	0.00016	0.02062	0.16633	0.000246	0.03089	0.249198
"Triple-nozzle"	0.000007	0.000396	0.00528	6.57E-05	0.004294	0.05296	0.000095	0.01217	0.09338	0.000144	0.018158	0.14972
"Quad-nozzle"	0.000011	0.00036	0.00291	0.000032	0.00349	0.02785	0.00005	0.00732	0.0604	0.00008	0.01099	0.09273

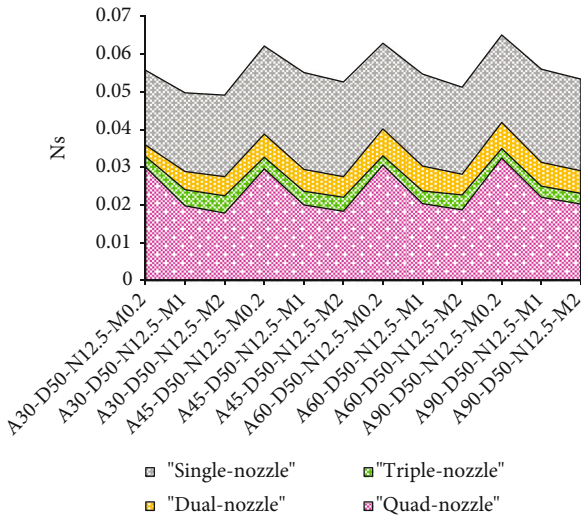FIGURE 4: Entropy generation due to frictional source.

FIGURE 5: Dimensionless entropy generation.

and mass flow rates can be seen in Figure 3. It is clear that the "single-nozzle" swirl generator has the highest entropy generation also as the number of nozzles increases entropy generations decreases. Moreover, the mass flow rate and the inclination angle of nozzles grow entropy generation increases. However, the effect of mass flow on the entropy generation augmentation is much more considerable than the injection angle of nozzles. Maximum amount of entropy generation is 428 J/K which is achieved by the case with a single nozzle and geometrical hydraulic specifications of "A60-D50-N12.5-M2." Conversely, the minimum entropy generation is 25 J/K which belongs to the case with four nozzles and specifications of "A30-D50-N12.5-M0.2."

Figure 4 shows the entropy generation caused by a frictional source. According to the results, as the angle of nozzles grow from 30° to 90°, the entropy generation increases. In fact, the growth of nozzles' angle pressure drop goes up where this causes augmentation in the entropy generation. In addition to the growth of injection angle, the increment of mass flow rate increases entropy generation. Moreover, increasing the number of nozzles declines the entropy generation. Based on the said definitions, maximum and minimum frictional entropy generation is 0.72 J/K and 0.011×10^{-3} J/K, respectively, caused by "single-nozzle; A90-D50-N12.5-M2" and "quad-nozzle; A30-D50-N12.5-M0.2."

4.2. Analysis of Dimensionless Parameters. Figure 5 presents the values of dimensionless entropy generation (Ns) for each of the cases. The behavior of dimensionless entropy generation is similar to total entropy generation with different values. In other words, the magnitude order of cases and parameters is same under all of the studied conditions. Only, there is a big difference, when mass flow rate increases entropy generation grows as well, while dimensionless entropy generation reduces. According to the presented results in Figure 5, the highest and the lowest dimensionless entropy generation is 0.065 and 0.0178, respectively, which are related to "single-nozzle; A90-D50-N12.5-M0.2 " and "quad-nozzle; A30-D50-N12.5-M2."

The ratio of modified Nu to unmodified Nu for all types of samples is provided in Figure 6. It can be seen "single-nozzle" case has great potential to improve Nu compared to others. Indeed, as the number of nozzles increases although entropy generation increases, heat transfer potential (Nu) increases as well. At the highest level, the Nu of
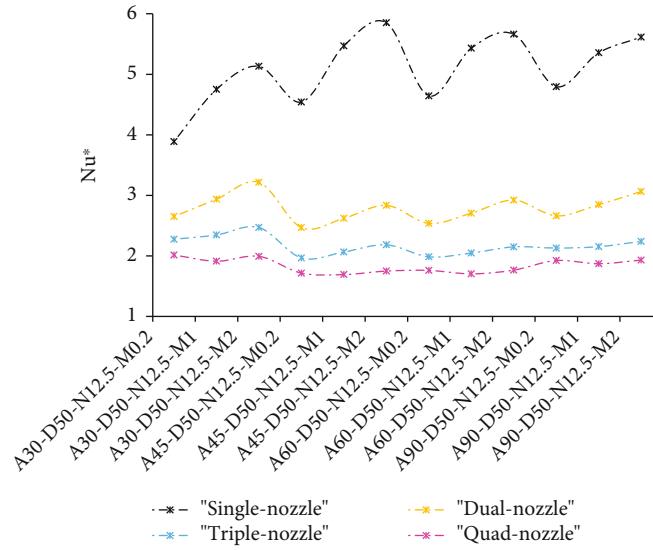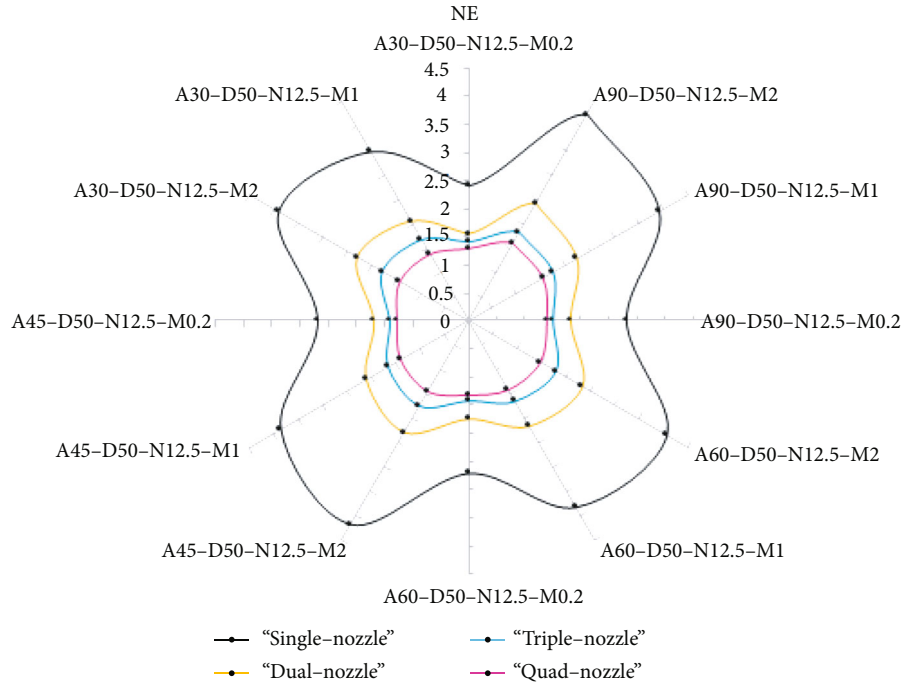
Figure 6: Ratio of modified Nu to unmodified Nu.

Figure 7: Ratio of modified N_s to unmodified N_s.

"single-nozzle" swirl generator (with the specification of "A45-D50-N12.5-M2") is about 5.85 times greater than a pipe with no swirl generator. As the number of nozzles reduces, the effect of mass flow rate on Nu* becomes considerable. Figure 7 shows the ratio of modified dimensionless entropy generation to the unmodified entropy generation (N_E). The magnitude order of samples of N_E is like Nu*. Comparing results of Nu* (Figure 6) and N_E (Figure 7) demonstrate that the enhancement of heat transfer of the designed swirl generators is greater than the augmentation of entropy generation. The maximum amount of N_E is 4.23 achieved by "single-nozzle; A90-D50-N12.5-M2."

Heat transfer improvement index (HTI) equals Nu*/N_E. The results of HTI are shown in Figure 8. Based on this parameter, it can be found that whether heat transfer improvement is greater than entropy generation number or not. According to Figure 8, all of the values of HTI are greater than unit where this implies that the ratio of Nu improvement is higher than entropy generation. Results show that the "single-nozzle" swirl generator has a higher HTI compared with others except for the inclination angle of 30°. Generally, the values of HTI are greater at the lower flow rates. Increasing nozzles cause the reduction of HTI. The maximum and minimum HTI is about 1.7 and 1.189
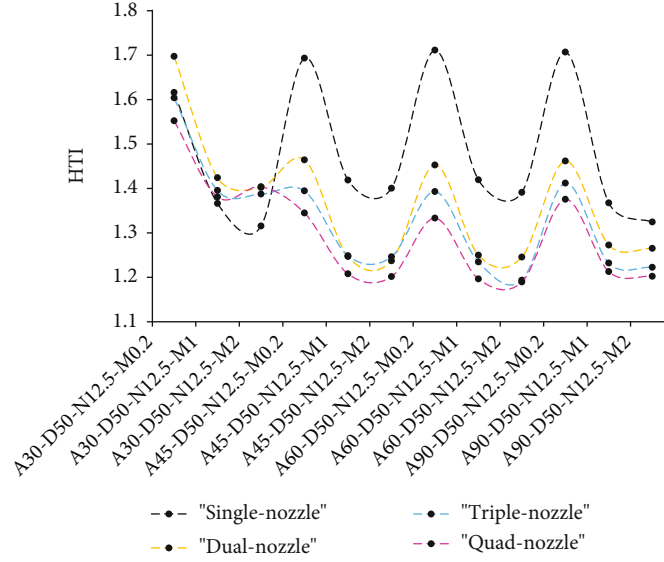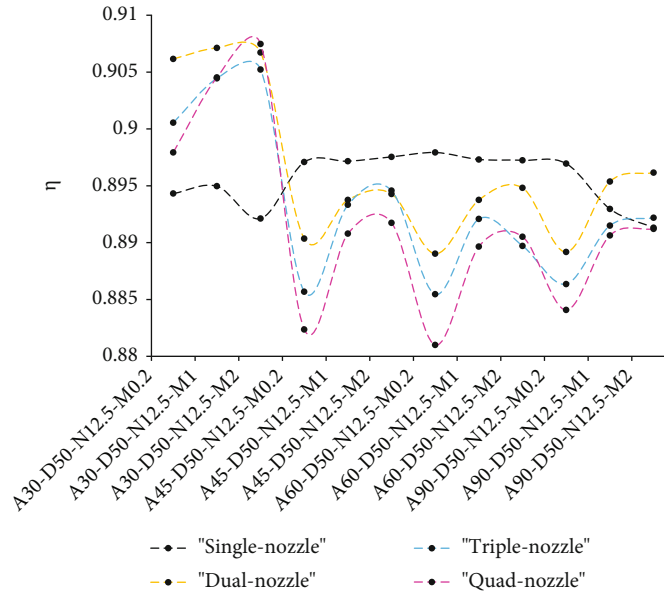
FIGURE 8: Heat transfer improvement index (HTI).

FIGURE 9: Witte-Shamsundar efficiency (η_{W-S}).

that can be obtained by "single-nozzle; A90-D50-N12.5-M0.2" and "quad-nozzle; A60-D50-N12.5-M2," respectively.

4.3. Witte-Shamsundar Efficiency (η_{W-S}) Analysis. Figure 9 provides the results of Witte-Shamsundar efficiency (η_{W-S}). As the values of η_{W-S} get close to unit, it shows that the quality of heat transfer is high, and the amount of generated irreversibility is low. Therefore, according to Figure 9, the highest η_{W-S} can be achieved when the nozzle inclination angle is 30°. Case "quad-nozzle; A30-D50-N12.5-M2" has the maximum η_{W-S} with a value of 0.9, while for the rest of the conditions, "quad-nozzle" swirl generator has the lowest η_{W-S}. When there is merely one nozzle, the value of η_{W-S} remains constant for injection angles of 45° and 60°. Also,

the injection angle is 45° and 60° with the addition of nozzles η_{W-S} that comes down.

5. Conclusion

The second law analysis of a pipe equipped with a swirl generator was done through numerical simulation. Number of nozzles was increased from one to four nozzles, and the inclination angle of them was varied from 30° to 90°. Irreversibility of all of the obtained designs was explored under three different mass flow rates. Results showed that by adding nozzles to the swirl generator, thermal and frictional entropy generation as well as HTI decreased. Furthermore, the increment of mass flow rate and injection angle

increased thermal and frictional entropy generation while decreased HTI. Interestingly, HTI values were higher than unit, and its maximum amount was 1.7 when case "single-nozzle; A90-D50-N12.5-M0.2" was tested. The swirl generator "quad-nozzle; A30-D50-N12.5-M2" made the highest η_{W-S} with a value of 0.9.

Nomenclature

"A":   Injection angle
C_P: Specific heat capacity (J/kg.K)
D: Diameter of pipe (mm)
"D":   Diameter (m)
f: Friction factor
h: Heat transfer coefficient (W/m^2.K)
K: Thermal conductivity (W/m.K)
L: Length of spiral pipe (mm)
$m\cdot$:   Mass flow rate (kg/s)
"M":   Mass flow rate (kg/s)
"N":   Nozzle cross-section edge (m)
Nu: Nusselt number
N_s: Dimensionless entropy generation ($S'_{gen}/ m\cdot C_p$)
N_E: Dimensionless number of exergy loss ($N_{s,a}/N_{s,s}$)
Nu^*:   Dimensionless form of the Nusselt number (Nu_a/Nu_s)
N_H: Heat transfer improvement number (Nu^*/N_E)
P: Pressure (Pa)
$Q\cdot$:   Heat transfer rate (J/s)
S'_{gen}:   Entropy generation rate (kJ/K)
Re: Reynolds number
T_0:   Ambient temperature (K)
T: Temperature (K)
ρ: Density (kg/m^3)
μ: Dynamic viscosity (kg/m.s)
u: Velocity (m/s)
g: Gravity acceleration (m/s^2)
η_{W-S}:   Witte-Shamsundar efficiency

Subscripts

r, θ, z: Axis direction of cylindrical coordinate system
f: Fluid
in: Inlet
out: Outlet
b: Bulk

Abbreviations

HTI index: Heat transfer improvement index
CFD: Computational fluid dynamic
FPSC: Flat plate solar collector.

Data Availability

Data are available on request.

Conflicts of Interest

The authors declare that they have no conflicts of interest.

References

[1] H. Li, B. Xu, G. Lu, C. Du, and N. Huang, "Multi-objective optimization of PEM fuel cell by coupled significant variables recognition, surrogate models and a multi-objective genetic algorithm," *Energy Conversion and Management*, vol. 236, p. 114063, 2021.

[2] X. Duan, B. Deng, Y. Liu, Y. Li, and J. Liu, "Experimental study the impacts of the key operating and design parameters on the cycle-to-cycle variations of the natural gas SI engine," *Fuel (Guildford)*, vol. 290, p. 119976, 2021.

[3] L. Sun, C. Li, C. Zhang, T. Liang, and Z. Zhao, "The strain transfer mechanism of fiber Bragg grating sensor for extra large strain monitoring," *Sensors (Basel, Switzerland)*, vol. 19, no. 8, p. 1851, 2019.

[4] H. Guan, S. Huang, J. Ding, F. Tian, Q. Xu, and J. Zhao, "Chemical environment and magnetic moment effects on point defect formations in CoCrNi-based concentrated solid-solution alloys," *Acta Materialia*, vol. 187, pp. 122–134, 2020.

[5] D. Zhu, B. Wang, H. Ma, and H. Wang, "Evaluating the vulnerability of integrated electricity-heat-gas systems based on the high-dimensional random matrix theory," *CSEE Journal of Power and Energy Systems*, vol. 6, no. 4, pp. 878–889, 2020.

[6] B. Zhang, Y. Chen, Z. Wang, J. Li, and H. Ji, "Influence of mach number of Main flow on film cooling characteristics under supersonic condition," *Symmetry (Basel)*, vol. 13, no. 127, p. 127, 2021.

[7] C. Liu, M. Hashemian, A. Shawabkeh et al., "CFD-based irreversibility analysis of avant-garde semi-O/O-shape grooving fashions of solar pond heat trade-off unit," *Renewable Energy*, vol. 171, pp. 328–343, 2021.

[8] Y. Cao, H. Ayed, M. Hashemian, A. Issakhov, and M. Waehayee, "Thermal/frictional performance of spiral pipe with ring-shape depression used as in-pond heat exchanger," *Solar Energy*, vol. 224, pp. 742–756, 2021.

[9] S. Jafary and S. Khalilarya, "A complete energetic and exergetic analysis of a solar powered trigeneration system with two novel organic Rankine cycle (ORC) configurations," *Journal of Cleaner Production*, vol. 281, p. 124552, 2021.

[10] A. Ahmadi, M. A. Ehyaei, A. Doustgani et al., "Recent residential applications of low-temperature solar collector," *Journal of Cleaner Production*, vol. 279, article 123549, 2021.

[11] S. Rahman, S. Issa, Z. Said, M. E. H. Assad, R. Zadeh, and Y. Barani, "Performance enhancement of a solar powered air conditioning system using passive techniques and SWCNT /R-407c nano refrigerant," *Case Studies in Thermal Engineering*, vol. 16, p. 100565, 2019.

[12] K. G. Kumar, E. H. B. Hani, M. E. H. Assad et al., "A novel approach for investigation of heat transfer enhancement with ferromagnetic hybrid nanofluid by considering solar radiation," *Microsystem Technologies*, vol. 27, no. 1, pp. 97–104, 2021.

[13] A. Khosravi, S. Syri, X. Zhao, and M. E. H. Assad, "An artificial intelligence approach for thermodynamic modeling of

geothermal based-organic Rankine cycle equipped with solar system," *Geothermics*, vol. 80, pp. 138–154, 2019.

[14] M. El Haj Assad, "Effect of maximum and minimum heat capacity rate on entropy generation in a heat exchanger," *International Journal of Energy Research*, vol. 34-14, pp. 1302–1308, 2010.

[15] M. E. H. Assad, "Thermodynamic analysis of an irreversible MHD power plant," *International Journal of Energy Research*, vol. 24, no. 10, pp. 865–875, 2000.

[16] M. E. H. Assad, Y. Aryanfar, S. Radman, B. Yousef, and M. Pakatchian, "Energy and exergy analyses of single flash geothermal power plant at optimum separator temperature," *International Journal of Low Carbon Technologies*, vol. 2021, article ctab014, 2021.

[17] M. A. Ehyaei, A. Ahmadi, M. El Haj Assad, A. A. Hachicha, and Z. Said, "Energy, exergy and economic analyses for the selection of working fluid and metal oxide nanofluids in a parabolic trough collector," *Solar Energy*, vol. 187, pp. 175–184, 2019.

[18] S. Pourhedayat, S. M. Pesteei, H. E. Ghalinghie, M. Hashemian, and M. A. Ashraf, "Thermal-exergetic behavior of triangular vortex generators through the cylindrical tubes," *International Journal of Heat and Mass Transfer*, vol. 151, p. 119406, 2020.

[19] M. Jalili, A. Chitsaz, M. Hashemian, and M. A. Rosen, "Economic and environmental assessment using emergy of a geothermal power plant," *Energy Conversion and Management*, vol. 228, p. 113666, 2021.

[20] Y. A. al-Turki, H. Moria, A. Shawabkeh, S. Pourhedayat, M. Hashemian, and H. S. Dizaji, "Thermal, frictional and exergetic analysis of non-parallel configurations for plate heat exchangers," *Chemical Engineering and Processing Process Intensification*, vol. 161, p. 108319, 2021.

[21] Y. Cao, H. Ayed, H. S. Dizaji, M. Hashemian, and M. Wae-hayee, "Entropic analysis of a double helical tube heat exchanger including circular depressions on both inner and outer tube," *Case Studies in Thermal Engineering*, vol. 26, p. 101053, 2021.

[22] Y. Cao, M. AliAbdous, S. G. Holagh, M. Shafiee, and M. Hashemian, "Entropy generation and sensitivity analysis of R134afFlow condensation inside a helically coiled tube-in-tube heat exchanger," *International Journal of Refrigeration*, vol. 130, 2021.

[23] H. Li, Y. Gao, C. Du, and W. Hong, "Numerical study on swirl cooling flow, heat transfer and stress characteristics based on fluid-structure coupling method under different swirl chamber heights and Reynolds numbers," *International Journal of Heat and Mass Transfer*, vol. 173, p. 121228, 2021.

[24] Z. Li, M. Peng, X. Zhou et al., "In situ chemical lithiation transforms diamond-like carbon into an ultrastrong ion conductor for dendrite-free lithium-metal anodes," *Advanced Materials*, vol. 33, no. 37, p. 2100793, 2021.

[25] X. Tong, F. Zhang, B. Ji, M. Sheng, and Y. Tang, "Carbon-coated porous aluminum foil anode for high-rate, long-term cycling stability, and high energy density dual-ion batteries," *Advanced Materials*, vol. 28, no. 45, pp. 9979–9985, 2016.

[26] Y. Cao, H. Ayed, M. Hashemian, A. Issakhov, F. Jarad, and M. Wae-hayee, "Inducing swirl flow inside the pipes of flat-plate solar collector by using multiple nozzles for enhancing thermal performance," *Renewable Energy*, vol. 180, pp. 1344–1357, 2021.

[27] S.-R. Yan, H. Moria, S. Pourhedayat et al., "A critique of effectiveness concept for heat exchangers; theoretical- experimental study," *International Journal of Heat and Mass Transfer*, vol. 159, article 120160, 2020.

[28] Y. Cao, H. Ayed, S. Jafarmadar et al., "PEM fuel cell cathode-side flow field design optimization based on multi- criteria analysis of liquid-slug dynamics," *Journal of Industrial and Engineering Chemistry*, vol. 98, pp. 397–412, 2021.

[29] F. Chang and V. K. Dhir, "Turbulent flow field in tangentially injected swirl flows in tubes," *International Journal of Heat and Fluid Flow*, vol. 15, no. 5, pp. 346–356, 1994.